J. Fluid Mech. (2005), *vol.* 536, *pp.* 185–207.
doi:10.1017/S0022112005004490 Printed in the United Kingdom

Vortex shedding in the near wake of a parachute canopy

By HAMID JOHARI AND KENNETH J. DESABRAIS

Mechanical Engineering Department, Worcester Polytechnic Institute, Worcester, MA 01609, USA

(Received 14 January 2004 and in revised form 16 February 2005)

The dynamics of flexible parachute canopies and vortex shedding in their near wake are studied experimentally in a water tunnel. The velocity field was measured by particle image velocimetry for two different canopy diameters. The periodic oscillation of the canopy diameter about a mean value which is referred to as 'breathing' has a non-dimensional frequency, based on the free-stream velocity and the mean canopy projected diameter, of approximately 0.55 for the range of Reynolds numbers examined. The dimensionless breathing frequency observed in the experiments is consistent with the values for larger canopies. The shear layer emanating from the canopy rolls up and sheds symmetric vortex rings. The frequency of vortex shedding was measured to be the same as the canopy breathing frequency. This Strouhal number is unique in the sense that it is much higher than those associated with rigid axisymmetric bluff bodies such as disks and spheres. The canopy breathing is shown to stem from the cyclical variation of suction pressure, resulting from the passage of vortex rings, on the exterior surface of the canopy. The added mass associated with the breathing of the canopy is found to be accountable for up to 40 % of the canopy drag fluctuations in the range of parameters investigated.

1. Introduction

Round parachute canopies pose challenging problems for the understanding of axisymmetric bluff-body wakes. Two features specific to fabric canopies differentiate them from rigid bluff bodies such as cups, disks or spheres. First, and most importantly, fabric flexibility allows large variations in the canopy geometry not only in the inflation phase, but also during terminal descent. Secondly, there is a small mean flow through the canopy surface owing to the fabric permeability, amounting to a few per cent of the free-stream velocity. Given that bluff-body wakes are unsteady, coupling of the time-dependent vortical flow in the near wake with the flexible fabric geometry results in strong fluid–structure interaction. Moreover, full-scale canopies operate typically at Reynolds numbers exceeding several millions. The complexity of these issues has so far precluded a thorough examination of the flow field in the near wake of parachute canopies. The flow structure in the near wake is also responsible for the aerodynamic forces and moments experienced by the canopy. We are interested in examining the dynamics of flexible canopies and the relationship between the near-wake flow field and the canopy motions. Since there is a general lack of data in the literature on the flow about flexible bluff bodies and rigid hemispherical shells, the key flow features in the wake of disk and sphere are presented below to provide a basis for comparison with the results of our study.

Vortex shedding from spheres in incompressible flow has been studied extensively. Numerical study of Natarajan & Acrivos (1993) indicates that the wake of a sphere becomes unstable at a Reynolds number of 105 and the primary unstable mode is non-axisymmetric, in concurrence with experimental observations. The structure of sphere wake is complex and Reynolds-number dependent. Visual observations have shown that vortices form a double helix (Pao & Kao 1977) or hairpin loops (Achenbach 1974; Sakamoto & Haniu 1990) at Reynolds numbers of $\sim 10^3$, whereas at Reynolds numbers of $\sim 10^4$ and beyond, the wake becomes completely turbulent with quasi-periodically spaced vortex loops or rings (Taneda 1978). The primary Strouhal number associated with vortex shedding in the sphere wake is ≈ 0.2 for Reynolds numbers greater than about 10^3 (Achenbach 1974; Kim & Durbin 1988; Sakamoto & Haniu 1990). Also, there is a higher-frequency mode close to the sphere at a Strouhal number that increases with Reynolds number (Kim & Durbin 1988). This mode is associated with the separated shear-layer vortices.

A circular disk is perhaps more representative of round canopies since the separation line is fixed at the disk edge, analogous to the location of separation line near the canopy skirt. Fuchs, Mercker & Michel (1979) and Berger, Scholz & Schumm (1990) have examined the flow structure in the disk wake at Reynolds numbers of $\sim 10^4$ using cross-spectral analysis at 3 and 9 disk diameters. Three instability modes have been identified: an axisymmetric oscillation of the recirculation bubble at a low Strouhal number of ≈ 0.05; a helical mode at a Strouhal number of ≈ 0.14; and a high-frequency mode at a Strouhal number of 1.6 associated with the separated shear layer. The mean recirculation bubble extends to about 2.5 diameters behind the disk. Flow visualization of Higuchi (1991) confirmed the primary helical mode at a Reynolds number of 10^4 in the disk wake. However, close-up observations in a water tunnel revealed that the tilting of vortex rings results in asymmetric structures after the first diameter in the disk wake. Smoke-flow visualization of Berger *et al.* (1990) also indicated the formation of axisymmetric vortex rings in the immediate vicinity of the disk; tilting and linking of the rings in the near wake create the helical structure.

The flow inside rigid cylindrical cups, with and without a central vent, was measured by Lamberson, Higuchi & van Rooij (1999). The flow became stagnant (without the central vent) or reduced to small velocities (with the vent) along the cup centreline. Near wake of rigid cup-like bluff bodies in uniform flow has not been examined in the past.

The characteristic features of parachute canopies during various phases from deployment to terminal descent have been reviewed by Peterson, Strickland & Higuchi (1996) and Strickland & Higuchi (1996). One of the features of the canopy dynamics during terminal descent is the 'breathing' of the canopy where the maximum diameter (typically at or near the skirt) oscillates about a mean value periodically. This is caused by the interaction of the near-wake fluid forces with the flexible low-inertia fabric. Similarly, the drag fluctuates about a mean value. Maydew & Peterson (1991) have summarized drag and surface pressure measurements on sub- and full-scale canopies. Moreover, limited near-wake flow measurements have been conducted using helium bubbles (Klimas & Rogers 1977) and particle tracking (Lingard 1978) in the inflation phase of laboratory-scale canopy models. However, no detailed measurements of the flow field in the near wake of flexible canopies in a uniform stream have been reported.

In this paper, we examine the breathing of flexible circular parachute canopies, flow structure and vortex shedding in the near wake, as well as the relationship between vortex shedding and the canopy dynamics. Our experimental approach uses

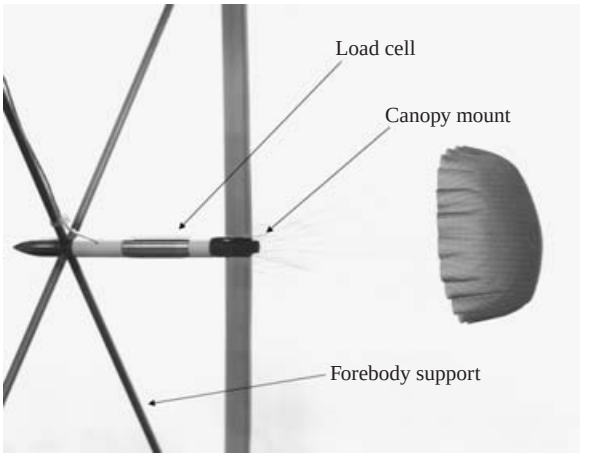

FIGURE 1. Forebody support structure and the 15 cm canopy in the water tunnel.

small-scale fabric model canopies in steady uniform flow. The experimental set-up is described in § 2, and the relevant dimensionless parameters are discussed in § 3. Results are presented and discussed in § 4.

2. Experimental set-up

The experiments were conducted in a water tunnel at free-stream velocities in the range $20 \leqslant U \leqslant 40\,\mathrm{cm\,s^{-1}}$. The free-stream turbulence intensity was measured to be less than 1.3 % over this operating range. The water-tunnel test section had a 0.6 m square cross-section and was 2.4 m long. Optical access was available through the transparent Lexan® test-section walls.

The inflated canopy in the water tunnel and the supporting hardware are shown in figure 1. The parachute assembly was positioned in a horizontal orientation. The canopy was attached by 24 suspension lines to a stationary streamlined forebody. The forebody had a diameter of 1.4 cm and a length of approximately 17 cm. The cross-sectional area of the forebody was less than 2 % of the canopy projected area. By streamlining the forebody and reducing its diameter, the forebody wake was kept to a minimum. The forebody was supported by four 0.64 cm diameter rods in the centre of the water-tunnel test section. Flow visualization confirmed that the wake of forebody support rods had a negligible effect on the parachute canopy geometry and dynamics.

A schematic diagram of an inflated canopy along with definitions of the relevant canopy parameters is shown in figure 2. The constructed diameter, D_o, refers to the diagonal extent along the canopy surface, while D_m is the maximum projected diameter. The axial extent (depth) of the canopy is denoted by H. The time-averaged projected diameter, D_p, is based on the mean canopy projected area. Both H and D_m vary periodically in time for round parachute canopies.

Two canopy models with constructed diameters of 15.2 cm and 30.5 cm were fabricated. The models were created from a flat circular pattern, without a central vent. The canopies were constructed from standard rip-stop nylon from one solid piece of fabric. This fabrication technique minimized stiffness of the model canopies. The 24 suspension lines were made from 100 μm diameter nylon thread and attached to a mount on the forebody (shown in figure 1). The length of suspensions lines

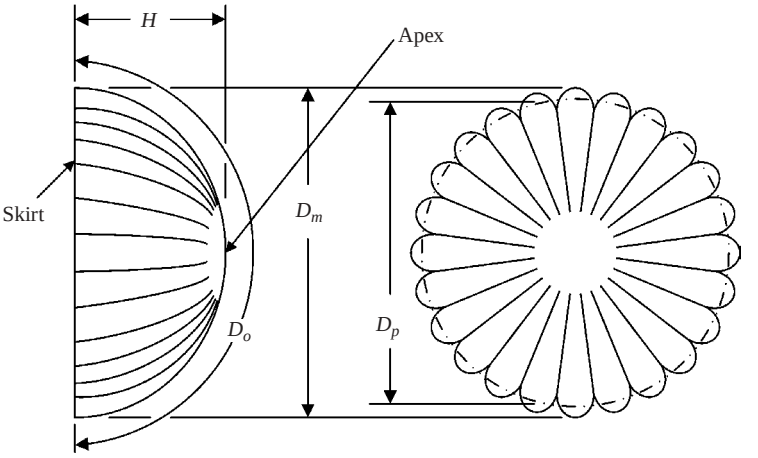

FIGURE 2. Schematic of a parachute canopy and the associated parameters.

Canopy	D_o (cm)	U (cm s^{-1})	Re	ε^{sb}(%)
Small	15.2	20	3.0×10^4	2.5
	15.2	25	3.7×10^4	2.5
	15.2	30	4.5×10^4	2.5
	15.2	35	5.2×10^4	2.5
	15.2	40	5.9×10^4	2.5
Large	30.5	20	6.0×10^4	9.9

TABLE 1. Reynolds number and solid blockage for the two models.

was equal to the constructed diameter. Full-scale personnel parachutes typically have about 30 suspensions lines.

Flat circular canopy geometries are known to have off-axis oscillations during terminal descent. Weber & Garrard (1982) noted statically stable trim angles of 10° for small ribbon parachute canopies. In order to eliminate the off-axis oscillations, a 500 μm diameter flexible nylon retention line was attached to the forebody and passed through the apex of the canopy. The end of the retention line was held rigidly far downstream of the canopy. The retention line restrained the canopy wandering without adversely affecting the flexible nature of the canopy. The presence of the retention line placed the canopy apex approximately 5° off centreline with respect to the forebody and free-stream.

The Reynolds number, $Re = U\,D_o\,/\nu$, for a parachute canopy is commonly based on the constructed diameter D_o (ν is the kinematic viscosity). Using the mean projected diameter would result in Reynolds numbers approximately 30 % smaller. Table 1 gives the Reynolds numbers as well as the tunnel solid blockage, ε^{sb}, for the two models. Standard methods for calculation of the blockage ratio for bluff bodies and parachute canopies in closed wind/water tunnels employ the projected area of the canopy divided by the tunnel cross-sectional area (Maskell 1965; Rae & Pope 1984; Cockrell 1987). Based on the mean projected diameters of 10.7 and 21.3 cm for the two models, blockage ratios are 2.5 % and 9.9 %, respectively. Cockrell (1987) states that blockage ratios up to 10 % can be readily corrected using Maskell's method. Macha & Buffington (1989) provide the following expression for the tunnel dynamic

pressure correction, based on Maskell's method. The dynamic pressure, q_o, was corrected by

$$q_o = q_{o_u}\left[1 + K_M \frac{C_{Du} S_p}{S_T}\right],$$

where q_{o_u} is the uncorrected dynamic pressure, K_M is an empirically derived blockage factor (see Macha & Buffington 1989), C_{D_u} is the uncorrected drag coefficient of the canopy, S_p is the projected area of the canopy diameter, and S_T is the cross-sectional area of the test section. The maximum dynamic pressure corrections were 2 % and 11.6 % for the 15 and 30 cm models, respectively. These values correspond to 1 % and 5.6 % corrections for the free-stream velocity.

Although the effects of blockage on shedding frequency of axisymmetric bluff bodies have not been investigated thoroughly in the past, West & Apelt (1982) have carried out a careful study of blockage on drag coefficient and shedding frequency of circular cylinders in the range of Reynolds numbers corresponding to those in the present experiments. They conclude that for blockage ratios less than 6 %, the effects of blockage on pressure distribution and the drag coefficient are small and the Strouhal number is not affected by blockage. West & Apelt (1982) state that the blockage effects become complex for blockage ratios up to 16 %. Their shedding-frequency data show a 2.3 % increase in the Strouhal number at a blockage ratio of 10 %. Thus, assuming that similar effects are present for an axisymmetric bluff body, the drag coefficient and the Strouhal number of our small model having a blockage of 2.5 % should not be affected by blockage. Moreover, an increase of only a few per cent is expected for the shedding frequency of the larger model with a blockage of 9.9 %.

Drag, F, on the canopy was measured by a load cell mounted inside the forebody and attached directly to the suspension lines. The load cell was sampled at 150 Hz with a 12-bit A/D card. The uncertainty of the drag measurement system was 0.027 N, or 0.4 % at full scale of the load cell. The load cell was calibrated *in situ* prior to and after each experiment.

Two types of experiment were conducted in the present study. The canopy geometry and drag were measured simultaneously in one set of experiments, while the velocity field and drag measurements were carried out in the other set of experiments. In the former set, the variations of the canopy geometrical parameters such as the diameter and depth were measured precisely. In the latter set, the velocity field was measured by the particle image velocimetry (PIV) technique. Even though the canopy surface could be extracted from the PIV images, the sampling rate and accuracy of canopy geometrical parameters was less than in the former set. The reduced accuracy was a result of the larger field of view and laser sheet illumination.

The canopy was imaged by a mega-pixel progressive-scan CCD camera with a 30 Hz frame rate. A 24 mm lens was used with a shutter speed of 1/250 s. The images were digitally transferred in real-time to a PC. The camera was positioned such that the side view of the parachute canopy appeared vertically oriented in the images. To measure the canopy perimeter, the test section was backlit by a floodlight through a white diffuser screen. This arrangement allowed for maximum contrast between the canopy and background for ease of image processing. An automated image-processing routine was developed to extract the maximum projected diameter, D_m, and the canopy depth, H, from each image. The measurement uncertainty of the maximum projected diameter and depth was 5 pixels $\approx 0.005\, D_o$. The details of the image processing routine can be found in Desabrais (2002).

Canopy	D_o (m)	Re	δ/D_o	$m/\rho D_o^3$	ζ
Small model	0.15	3.0×10^4	4.7×10^{-4}	2.1×10^{-4}	1.3×10^{-3}
Large model	0.30	6.0×10^4	2.3×10^{-4}	1.1×10^{-4}	1.6×10^{-4}
T-10	10.7	4.2×10^6	6.7×10^{-6}	4.1×10^{-3}	3.3×10^{-9}
G-12	19.5	1.1×10^7	3.6×10^{-6}	6.6×10^{-3}	2.5×10^{-10}

TABLE 2. Primary dimensionless parameters for laboratory and full-scale circular canopies.

In the PIV experiments, the entire water tunnel was seeded with neutrally buoyant silver-coated glass spheres with an average diameter of 46 μm. The flow was illuminated by a 3 mm thick sheet of laser light. The light source was a pair of pulsed Nd:YAG lasers, each operating at 15 Hz. The laser pulse separation was in the range of 3–6 ms. The CCD camera described above was used for PIV imaging, and the imaged area was $20 \times 20\,\text{cm}^2$ and $24 \times 24\,\text{cm}^2$ for the smaller and larger canopies, respectively. The data field extended from just upstream of the canopy to $\sim 1.7\,D_p$ downstream for the smaller canopy, and to $1.0\,D_p$ for the larger canopy.

The cross-correlation technique was used to process the PIV images (Willert & Gharib 1991; Raffel, Willert & Kompenhans 1998), resulting in a velocity field sampling rate of 15 Hz. The image pairs were processed with a window size of 32×32 pixels, and 75 % window overlap. The resulting vector spacing was 1.7 and 2.0 mm for the 15 and 30 cm canopies, respectively. For the cases in table 1, 1000 instantaneous velocity fields were acquired. The azimuthal vorticity, ω, was calculated from the velocity using a method outlined in Raffel *et al.* (1998). The average vorticity at a grid point is estimated by evaluating the circulation around the eight neighbouring points and dividing by the area enclosed by the eight points. Based on the sub-pixel accuracy of the cross-correlation peak and particle displacements in the near wake, the uncertainties in measured velocity and computed vorticity are estimated to be 3 % and 8 %, respectively.

3. Dimensionless parameters

The primary dimensionless parameters relevant to a parachute canopy in steady incompressible flow are the Reynolds number, fabric thickness ratio, canopy mass ratio, a stiffness index, and permeability ratio (Lingard 1978; Lee 1989; Johari & Desabrais 2003). Accounting for the entire parachute system including the payload would further increase the number of dimensionless parameters notably. The large number of dimensionless parameters precludes complete similarity at geometrical scales significantly smaller than full-scale canopies using the same fabric. Thus, the relative significance of each of the aforementioned dimensionless parameters (given in table 2) needs to be addressed. The parameters for the US Army's 35 feet (10.7 m) T-10 and 64 feet (19.5 m) G-12 parachutes are also given in table 2.

Reynolds numbers of the small canopy models are two to three orders of magnitude smaller than those of the full-scale canopies. It is commonly thought that the Reynolds number may not significantly affect the large-scale flow in the near wake when the flow is completely separated over the canopy exterior surface. This occurs once the Reynolds number exceeds several thousand. Knacke (1992) has shown that Reynolds number has little effect on the drag of a canopy over the range $10^5 < Re < 10^6$. Similarly, the drag coefficient and wake dynamics of a disk are Reynolds-number independent for values greater than $\sim 10^3$ (Hoerner 1965; Berger *et al.* 1990). Thus,

the large-scale flow structure in the near wake is expected to be mostly independent of Reynolds number.

Relative thickness of the canopy is characterized by δ/D_o, where δ is the fabric thickness. Because of the large diameters and thin fabrics used in a canopy, the thickness ratios in table 2 are quite small for the model and full-scale canopies. Even though the thickness ratios of model canopies are larger than their full-scale counterparts by about two orders of magnitude, they are still small enough to render the canopy effectively a two-dimensional surface.

Canopy mass ratio $m/\rho D_o^3$, where m is the canopy mass and ρ is the fluid density, is an indicator of the inertia of the canopy fabric. Because of the large density of water and the small mass of model canopies, the mass ratios of model canopies are even smaller than those for the full-scale canopies. The small values given in table 2 indicate that both model and full-scale canopies have relatively low inertia and respond rapidly to the imposed forces and motions. Although the canopy mass ratio is a dominant factor in the inflation phase, it does not appear to have a major impact during the terminal descent phase.

The response of a canopy to the imposed forces depends on both the mass ratio and a parameter specifying the material stiffness. Though different stiffness indices have been proposed in the literature (Heinrich & Hektner 1971; Niemi 1990), we will use Niemi's relative stiffness index $\zeta = (E/\rho U^2(1-\upsilon^2))(\delta/D_o)^3$, where E and υ are the fabric modulus of elasticity and Poisson's ratio, respectively. Since nylon fabrics used in the construction of parachute canopies possess a complex stress–strain relationship, data from uniaxial tests performed on nylon fabrics in the two in-plane directions were used. The moduli in the two in-plane directions were averaged and used as an equivalent modulus of elasticity. The numerical values of ζ in table 2 are based on the equivalent modulus of elasticity and Poisson's ratio presented by Niemi (1990).

The relative stiffness index ζ contrasts the strength of the fabric against the free-stream dynamic pressure. The values in table 2 indicate that the small models are six orders of magnitude stiffer than the full-scale canopies. Johari & Desabrais (2003) have shown that canopy dynamics during the inflation phase is a weak function of ζ. For example, normalized peak forces increase by a factor of 2 and opening times reduce by a factor 3 when ζ increases by 7 orders of magnitude from the full-scale values. Moreover, Weber & Garrad (1982) have shown that stiffness does not strongly affect the stability of parachute canopies. Thus, we expect that the stiffness index plays a small role during terminal descent since the canopy is fully open and the relative motion of the canopy is significantly smaller than during the inflation.

Nylon fabrics used in parachute canopies are permeable, producing a net flow through the fabric under an imposed pressure differential. Permeability is characterized by an average velocity c across the canopy fabric; this velocity depends on the fabric pore size and the pressure differential across the fabric. Permeability could possibly affect large-scale vortical motions behind bluff bodies. The dimensionless permeability ratio c/U is 1–2 % in our water-tunnel experiments, and 3–4 % during the terminal descent of full-scale canopies (Lingard 1978). The permeability ratio of the models in our set-up is thus fairly close to that of full-scale canopies.

Among the abovementioned parameters, the stiffness index and Reynolds number are the ones that differ greatly between full-scale and model canopies. While the Reynolds number affects the smaller scales and the flow in close proximity to the canopy surface, stiffness is responsible for the overall geometry and the response of the canopy to the imposed forces. As is shown in the next section, the mean projected diameter and depth of the model canopies is close to the full-scale values.

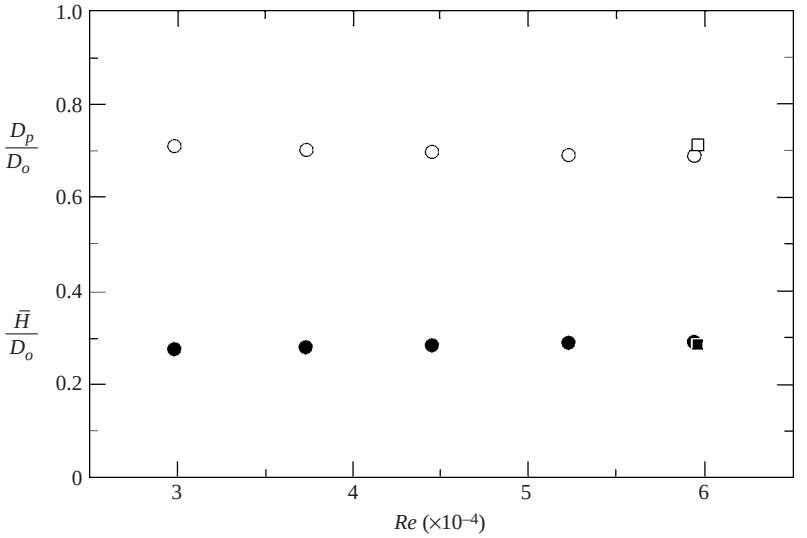

FIGURE 3. Average projected canopy diameter (open symbols) and depth (filled symbols) as a function of Reynolds number. Circle and square symbols denote the 15 and 30 cm canopies, respectively.

The normalized breathing frequency of full-scale canopies is also within 10 % of the laboratory values. Consequently, even though complete similarity cannot be achieved in our experiments, the use of incomplete similarity appears to be justified, at least as it relates to the large-scale dynamics in the near wake.

4. Results

The results are presented in terms of the canopy geometry first, followed by the average flow field, vortex shedding, near-wake structure, and drag measurements.

4.1. *Canopy dynamics*

To assess the changes in the canopy geometry, the maximum diameter D_m and depth H were extracted from the canopy images. The time-averaged depth $\bar{H}$ and projected diameter D_p are plotted in figure 3. The data reveal that both geometrical parameters remain constant over the range of Reynolds numbers in the experiment. Moreover, the average diameter of $D_p \approx 0.71 D_o$ is consistent with the range of 0.67–0.70 D_o reported for full-scale canopies (Knacke 1992). The average canopy depth of $\bar{H} \approx 0.28$ $D_o = 0.40$ D_p is also close to the $0.41 D_p$ for the full-scale canopies. The correlation coefficient between the projected diameter and canopy depth was in the range of -0.9 to -0.8 for all cases except at $Re \approx 6 \times 10^4$ where it was -0.5. The high negative correlation indicates that as the canopy expands, its depth decreases (and vice versa). The variation in the canopy geometry is restricted by the fixed canopy surface area. The reduced correlation at the higher Reynolds number was due to loss of symmetry of the canopy geometry.

The fluctuations of maximum diameter for the 15 cm canopy at $Re \approx 4.5 \times 10^4$ is shown in figure 4(*a*). The data clearly indicate a periodic motion associated with the canopy breathing. Similar time series were observed for all conditions given in table 1. The root mean square (r.m.s.) amplitude of diameter fluctuations is 3–5 % of the mean projected diameter, and the peak values are typically 7 % of D_p. Spectral analysis

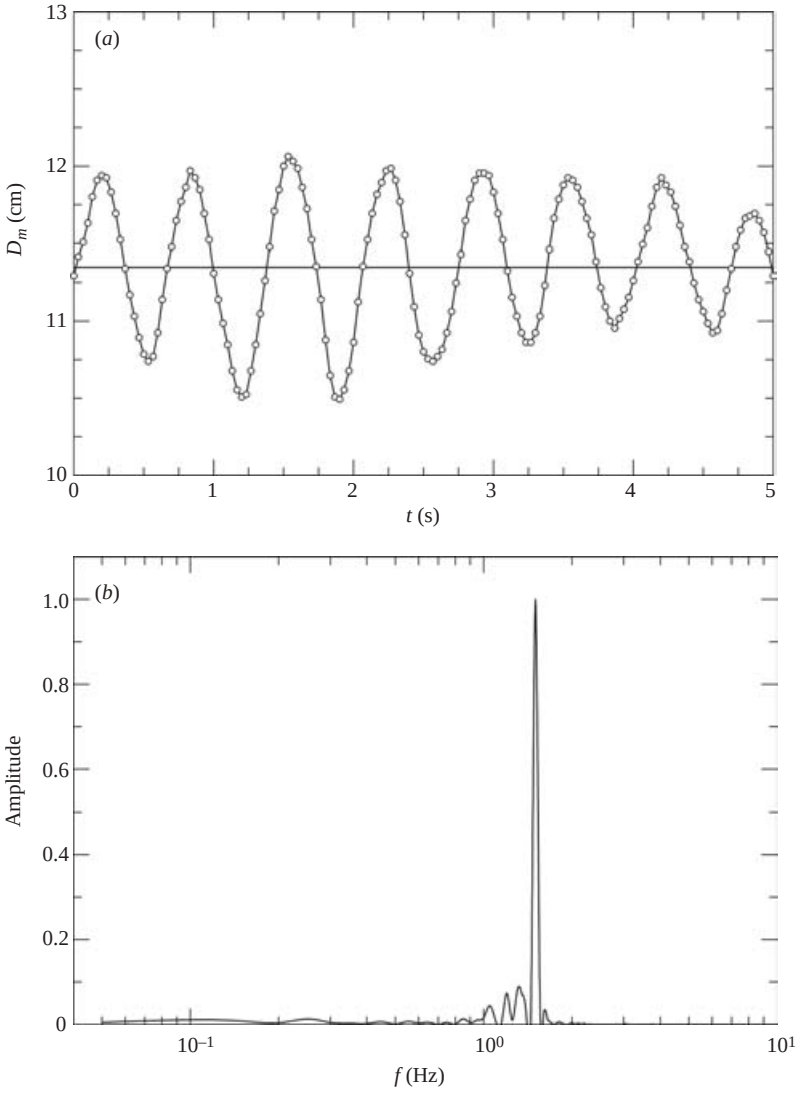

FIGURE 4. (*a*) Temporal variation of the maximum canopy diameter and (*b*) normalized spectrum for the 15 cm model canopy at $Re \approx 4.5 \times 10^4$.

of the time series shows a single primary peak at 1.5 Hz in figure 4(*b*). Normalizing this breathing frequency f_b with the free-stream velocity and the mean projected diameter results in a value of $f_b D_p / U \approx 0.55$. The normalized breathing frequency for various conditions is presented in figure 5. For the range of Reynolds numbers in our experiment, the normalized breathing frequency is nearly constant at $\approx 0.55 \pm 0.03$.

To check how the normalized frequency of our small-scale models compares with that of full-scale canopies, the average periods of breathing cycles for the 10.7 m T-10 and 19.5 m G-12 parachute canopies were measured from video sequences. The average breathing period for T-10 was 2.3 s, resulting in a normalized breathing frequency of 0.51 ($\pm 12\,\%$). The normalized breathing frequency for the larger G-12 canopy was 0.50 ($\pm 16\,\%$). The rather large standard deviations stem from the

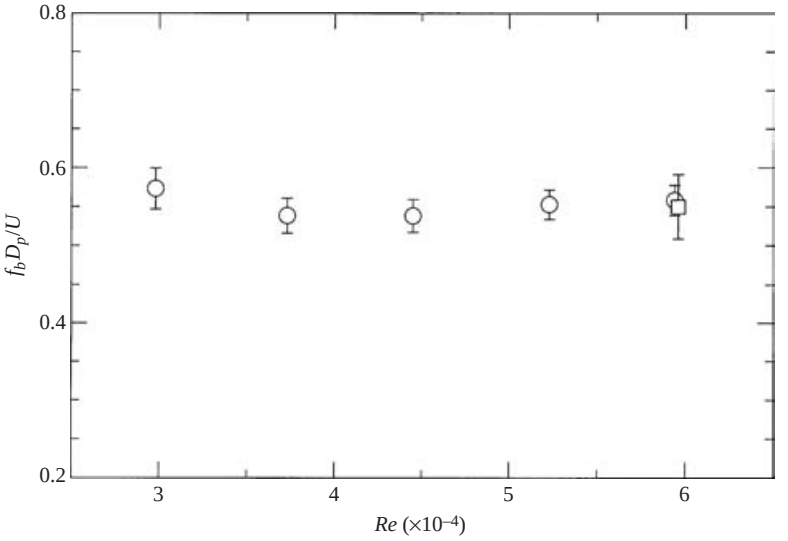

FIGURE 5. Normalized canopy breathing frequency as a function of Reynolds number. Circle and square symbols denote the 15 and 30 cm canopies, respectively.

uncontrolled environmental conditions during testing as well as the uncertainties in the measured projected diameter and terminal speed. The normalized breathing frequency of our models is within 10 % of these values, indicating that the breathing phenomenon is only weakly dependent on the stiffness and Reynolds number.

Inspecting the instantaneous vorticity fields for a number of breathing cycles revealed that the canopy attains its minimum diameter when the rolled-up vortex cores were in the range of $0.5\,D_p \leqslant z \leqslant 0.7\,D_p$, with the majority located at $z \approx 0.6\,D_p$. Maximum canopy diameter occurred when the rolled-up vortex cores were not present in the immediate vicinity of the canopy surface and the shear layer had not rolled up into a new vortex ring. Thus, the passage of low-pressure vortex cores in the near wake is responsible for the canopy breathing motions. Vortex shedding and phase-locked vorticity fields are discussed in the following sections.

4.2. *The mean flow*

The mean velocity field was obtained by averaging 1000 instantaneous fields. For the 15 cm canopy at $Re \approx 3.0 \times 10^4$, the averaging period corresponds to approximately 67 breathing cycles. The streamlines and normalized vorticity field $(\omega D_p/U)$ corresponding to the time-averaged flow field are presented in figure 6. The canopy outline is the average of all the instantaneous ones. The lower left-hand corner of the images resulted in poor correlation during the PIV processing (owing to reduced laser intensity), and affected data were removed. The near wake is characterized by a recirculation bubble; curvature of the streamlines outside the bubble is noteworthy. The mean vorticity field consists of a shear layer that separates near the canopy skirt, and decays rapidly downstream. Secondary vorticity of opposite sign, visible just above the canopy surface, is a result of the adverse pressure gradient imposed by the passage of vortices close to the canopy surface. The asymmetry appears to be due to the 5° misalignment of the canopy apex.

Radial profiles of the time-averaged axial velocity u and azimuthal vorticity ω are plotted in figure 7 at $z = 0.25$, 0.5, 1.0 and $1.5\,D_p$ axial locations. Since the canopy depth is $\approx 0.4\,D_p$, the profile at $0.25\,D_p$ does not extend to the wake centreline. Also,

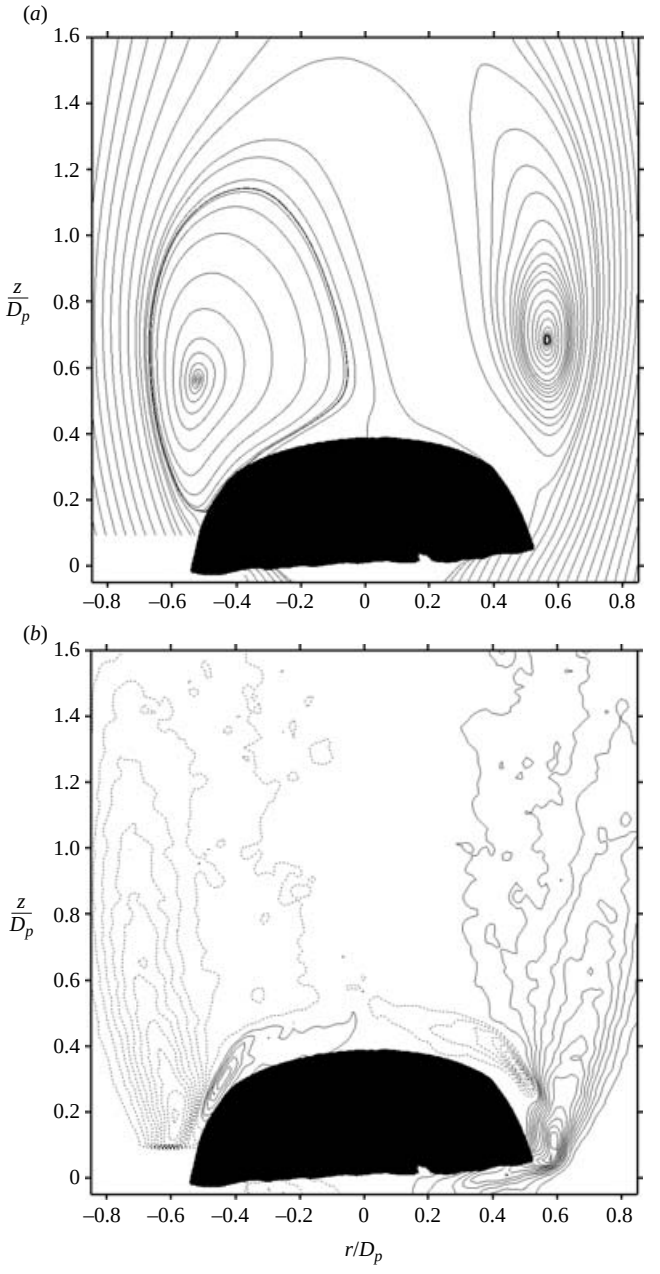

FIGURE 6. (*a*) Time-averaged streamlines and (*b*) vorticity contours for the 15 cm canopy at $Re \approx 3.0 \times 10^4$. The lowest vorticity contour is at $|\omega D_p/U| = 1.0$ with increments of 1.0. The time-averaged canopy outline is superimposed on the plots.

owing to the close proximity of the profile at $0.5\,D_p$ to the canopy apex, this velocity profile has a bump over the centreline. The radial velocity (not shown) is outward up to $z \sim 0.8\,D_p$, and inward thereafter owing to the growth of the wake. As the shear layer evolves downstream, the peak vorticity decays and the layer width increases. The largest vorticity in the shear layer is at $r \sim 0.6\,D_p$ near the canopy surface and

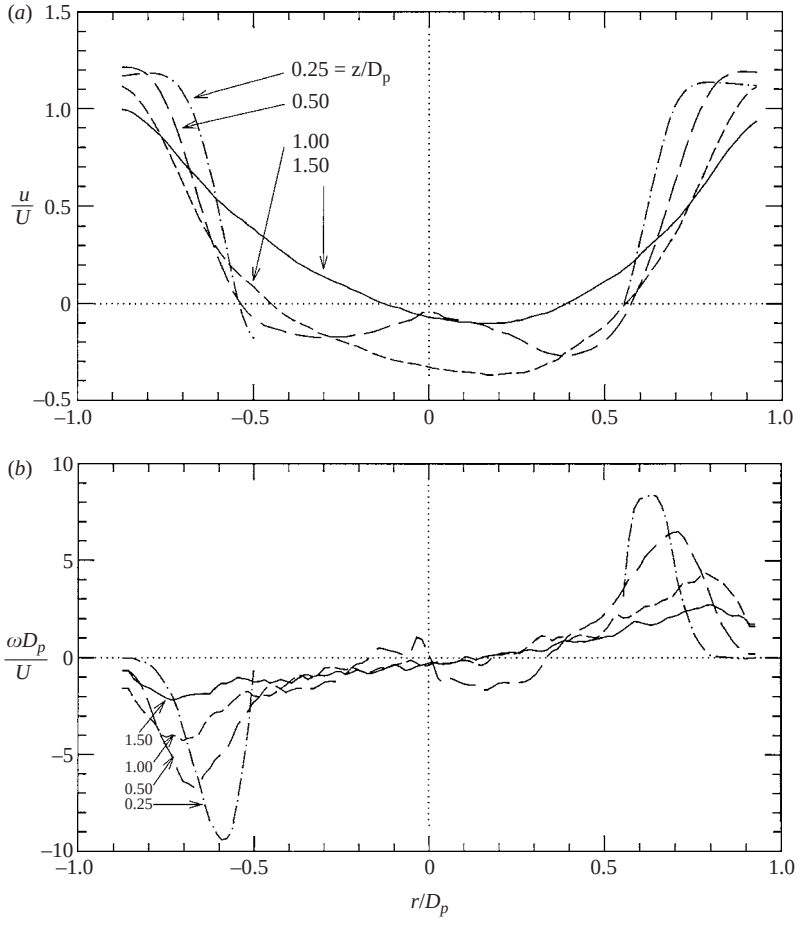

FIGURE 7. (*a*) Radial profiles of the axial velocity and (*b*) vorticity for the 15 cm model canopy at $Re \approx 3.0 \times 10^4$. The axial location of the profiles are noted on the plots.

moves out radially to $r \sim 0.8\,D_p$ near the end of the data field. The axial velocity on the centreline is plotted in figure 8. The negative values in the near wake indicate the reverse velocity in the recirculation bubble. The axial velocity decreases to $-0.36\,U$ at $z \sim 0.85\,D_p$, and it recovers to positive values for $z > 1.6\,D_p$. The mean velocity and vorticity profiles in the canopy near wake are generally consistent with those associated with rigid bluff bodies.

4.3. *Vortex shedding*

Vortex shedding in the near wake of model canopies was examined from the Eulerian (with a fixed probe in space) and Lagrangian (tracking of individual vortex formation and movement) perspectives. The results are discussed below.

To examine the passage of vortices in the near wake, the radial velocity v at specific locations (given in table 3) was extracted from the PIV datasets. The radial velocity was chosen because it has a larger dynamic range than the axial velocity. Three axial locations of $z = 0.25$, 1.0, 1.6 D_p, corresponding to a range extending from the canopy proximity to the end of the dataset, were chosen. The radial positions given in table 3 are based approximately on the locations where the largest radial velocities were present in the average field.

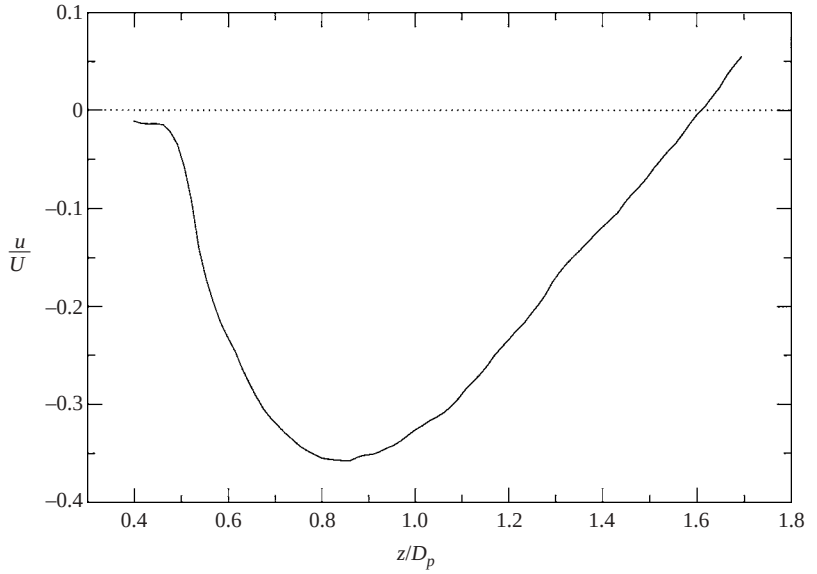

FIGURE 8. Axial velocity along the centerline. The canopy apex is at $z \approx 0.40\, D_p$.

D_o (cm)	z/D_p	r/D_p
15.2	0.25	$\pm$0.69
15.2	1.0	$\pm$0.81
15.2	1.59	0.81
30.5	0.25	0.69
30.5	0.97	0.97

TABLE 3. Radial velocity probe locations.

The radial velocity traces for the 15 cm canopy at the $z = 0.25\, D_p$ is shown in figure 9. Each trace corresponding to one side of the canopy has a quasi-periodic character. The traces for locations farther downstream and for all conditions in table 1 are comparable. Spectral analysis of such traces for the 15 cm canopy at the closest and farthest axial locations is shown in figure 10. In both spectra, there is a prominent peak (marked by the arrows) at a Strouhal number $St \equiv f\, D_p/U$ of approximately 0.55 corresponding to the breathing frequency of the canopy. This peak was observed for all the conditions given in table 1, and the average Strouhal number across the range of Reynolds numbers in our experiments was 0.54 ± 0.04. Even though a peak exists at a Strouhal number matching the canopy breathing frequency, there are other distinct peaks. At the point closest to the canopy (figure 10*a*), there is a sharp peak corresponding to twice the breathing frequency (i.e. a higher harmonic), and a broader low-amplitude peak centred about a Strouhal number of 0.16.

The peaks at the farthest location ($z = 1.6\, D_p$) are at Strouhal numbers of 0.16, 0.36 and 0.58. Aside from the canopy breathing frequency peak, the broad peak at $St \approx 0.16$ is similar to the $St \approx 0.14$ associated with the disk wake in the same Reynolds-number range (Berger *et al.* 1990). The other peak at $St \approx 0.36$ appears to be an aliasing artefact since it is halfway between the canopy breathing frequency at 0.55 and that at 0.16. The appearance of the $St \approx 0.16$ mode at this location is

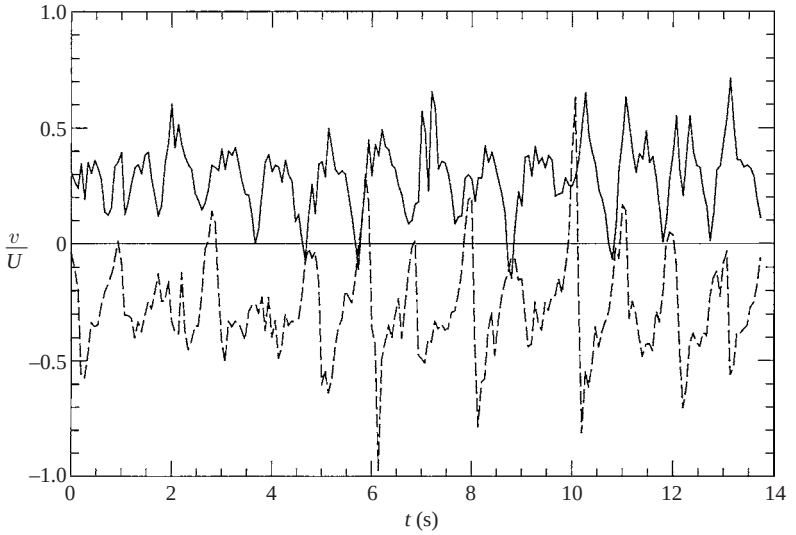

FIGURE 9. Time traces of the radial velocity for the 15 cm canopy at $Re \approx 3.0 \times 10^4$. $z/D_p = 0.25$; $r/D_p = +0.69$ (solid) and -0.69 (dashed).

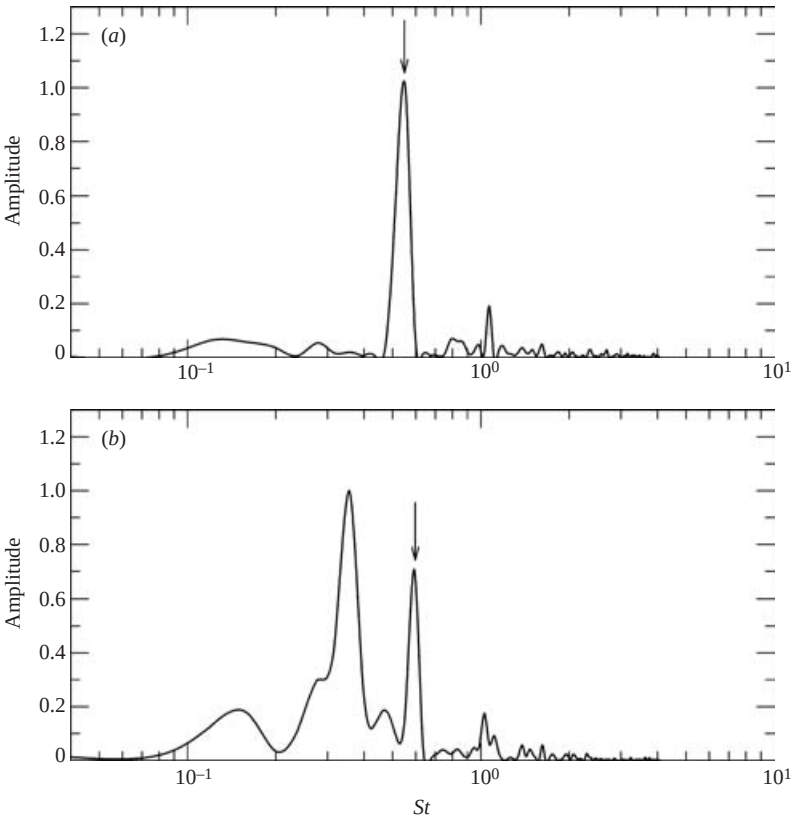

FIGURE 10. Spectra of radial velocity fluctuations for the 15 cm canopy at $Re \approx 3.0 \times 10^4$. (*a*) $z/D_p = 0.25$, $r/D_p = 0.69$; (*b*) $z/D_p = 1.59$, $r/D_p = 0.81$. Arrows indicate the peak associated with the breathing frequency.

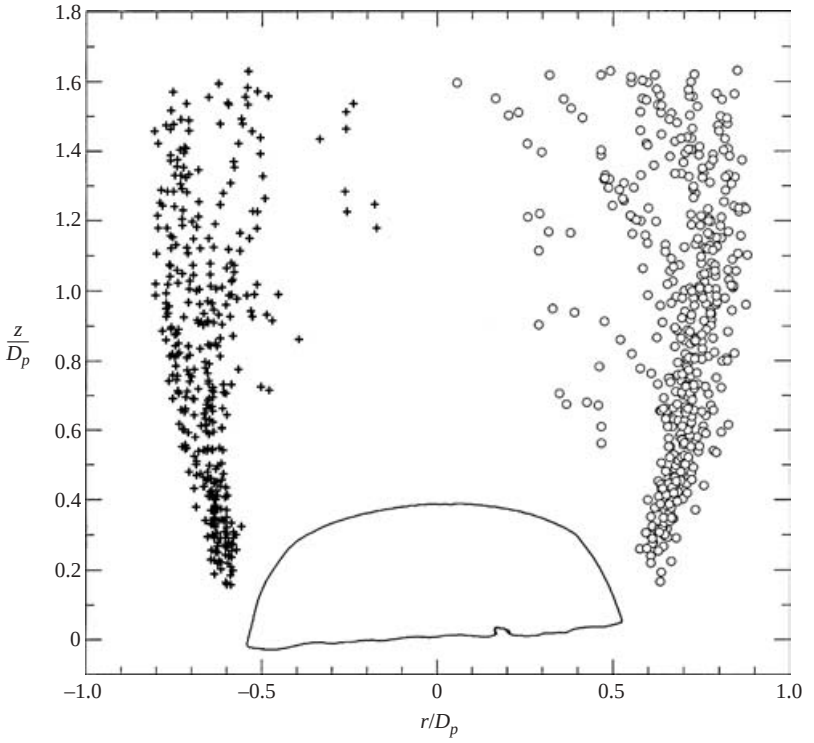

FIGURE 11. Trajectory of the vortex cores over 14 shedding cycles for the 15 cm canopy at $Re \approx 3.0 \times 10^4$. The average canopy outline is shown.

consistent with it becoming the prominent peak at $z = 3$ and 9 D in the disk studies of Fuchs *et al.* (1979) and Berger *et al.* (1990). These spectra indicate that apart from the breathing frequency associated with the canopy motions, the flow possesses a mode at a frequency of $St \approx 0.16$. This mode appears to be the asymmetric mode observed farther downstream in past studies.

An alternative means for examining vortex shedding from a canopy is to track the individual vortices formed in the near wake. The position of vortex cores was measured from the instantaneous PIV datasets by passing a Gaussian kernel over the vorticity field and locating the peak (positive and negative) vorticity. The location of vortex cores in the wake of the 15 cm canopy at $Re \approx 3.0 \times 10^4$ is shown in figure 11 for a period of 14 breathing cycles. Very close to the canopy, the peak vorticity is associated with the shear layer that has not rolled-up yet. The trajectory of vortex cores indicates a fairly repeatable roll-up process near the canopy, followed by the expansion of the wake as the vortices move downstream. The wake growth is evident by the increase in the width of the mean vortex position at the locations further downstream. Examination of individual vortex core traces revealed that symmetric vortex rings are formed in the shear layer. The vortex rings are then shed into the wake once they reach an axial location of about 1 D_p. Beyond this location, individual vortex rings lose their coherence and begin to tilt away from the centreline.

A time trace of the axial position of vortex cores for four breathing cycles is presented in figure 12 for the 15 cm canopy at $Re \approx 3.0 \times 10^4$. The periodic formation and shedding of vortices is indicated by the sawtooth pattern in the data. The vortex cores are only tracked until a stronger vortex emerges upstream. After that, the newer

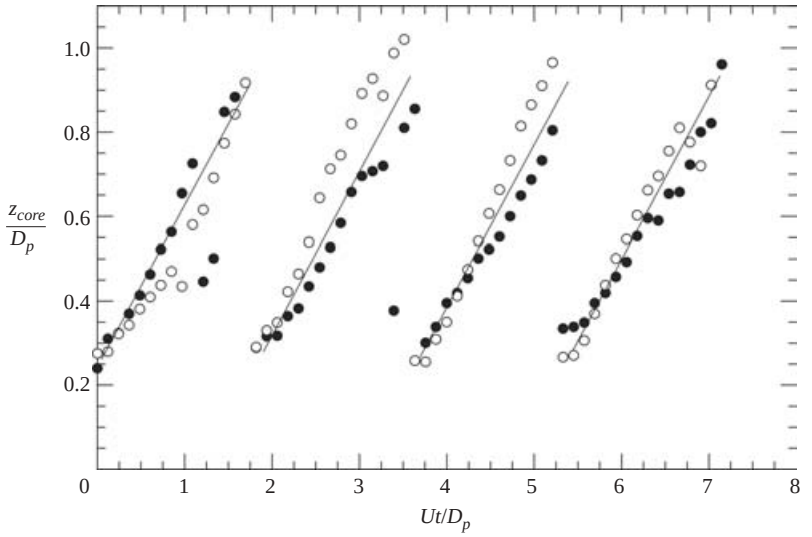

FIGURE 12. Temporal variation of the vortex core axial location for the 15 cm canopy at $Re \approx 3.0 \times 10^4$. Four breathing cycles are depicted.

vortex is tracked. The linear patterns in figure 12 reveal a nearly constant vortex celerity in the near wake. The average celerity of vortex cores, calculated from the slope of the linear portions in figure 12, is $0.41\,U$ ($\pm 5\,\%$). The average period of the sawtooth pattern for the entire dataset associated with figure 12 is $1.8\,D_p/U$ ($\pm 7\,\%$), corresponding to a vortex shedding frequency of $0.55\,U/D_p$. This is in agreement with the Strouhal number found from the spectral analysis of the radial velocity data. In addition, the close correspondence between the axial location of the left and right vortex cores indicates the initial symmetry of the vortex ring, at least in $z/D_p < 1$. This symmetry degrades at locations further downstream, and as Reynolds number increases.

The Strouhal number of 0.55 found in the near wake of flexible canopies is unique in the sense that it is much higher than the reported shedding frequencies for rigid disks ($St \approx 0.14$) and spheres ($St \approx 0.2$) at similar Reynolds numbers. We believe this is due to the low-inertia flexible canopy being forced synchronously by the roll-up and shedding of the vortices in the shear layer. Although the disk shear layer also rolls up symmetrically (Berger *et al.* 1990), there is no mechanism for the separation point, which is fixed at the disk edge, to respond to the imposed pressures. On the other hand, the separation point on the canopy, which is near the skirt, moves in space as a result of the canopy motions. Away from the canopy surface, we expect the vortex rings to tilt and link forming helical motions similar to those observed in rigid axisymmetric bluff bodies. The high-frequency mode associated with the shear layer of spheres is also different from the breathing frequency reported here since the former is at much higher Strouhal numbers (approximately a factor of 4 larger at similar Re) and is strongly Reynolds-number dependent (Kim & Durbin 1988). Thus, the Strouhal number of 0.55 appears to be unique to flexible canopies, and has not been observed previously in rigid bluff-body studies.

4.4. *Near-wake structure*

To examine structure of the canopy near wake and to identify the coherent vortical motions, the data fields were phase-averaged. The vortex-shedding/breathing cycle

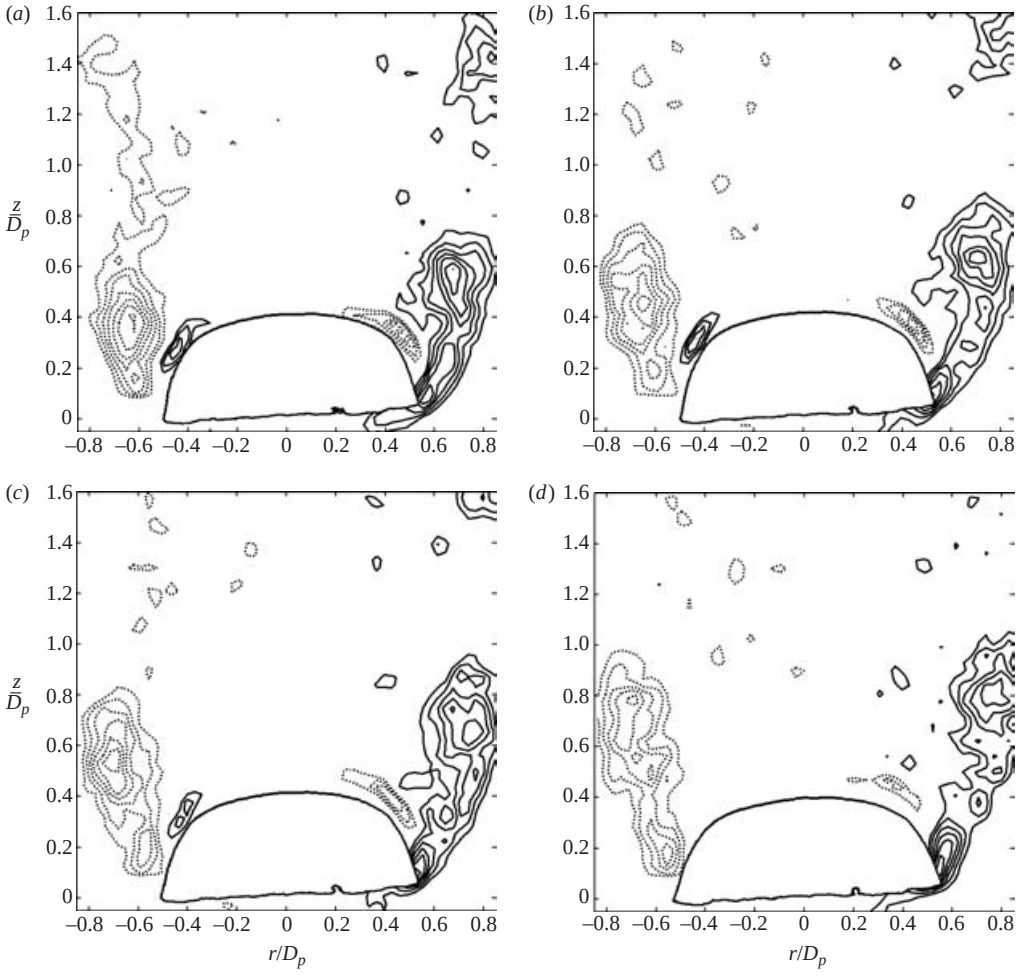

FIGURE 13(*a–d*). For caption see next page.

was divided into 15 equally spaced phases (for the 15 cm canopy at $Re \approx 3.0 \times 10^4$). The choice of 15 phases was dictated by the PIV sampling rate of 15 Hz and the breathing cycle having a period of 1 s.

Vorticity fields for eight of the 15 phases are shown in figure 13; the canopy outline shown is also a phase average of the canopy geometry. Data in the lower left-hand corner have been removed as noted earlier. The roll-up of the shear layer into a vortex ring and the eventual shedding of the ring is evident in this sequence. Figure 13(*f*) shows the phase at which the rolled-up vortex has completely separated from the shear layer and the vortex core is located at $\sim 1\, D_p$. The canopy has its maximum diameter at this point in the breathing cycle. Subsequently, the pinched-off vortex moves downstream and a new vortex rolls up in the shear layer. Appearance of opposite-signed vorticity between the shear layer and the canopy surface, owing to the imposed adverse pressure gradient, is indicative of a rolled-up vortex in the shear layer. Such opposite-signed vorticity (dashed contours underneath solid contours and vice versa) is discernible in figure 13(*a–c*, *g*, *h*). Furthermore, the nearly symmetric nature of the vortex ring formation and shedding can be seen at various phases in figure 13. Similar features were also observed for the 30 cm canopy.

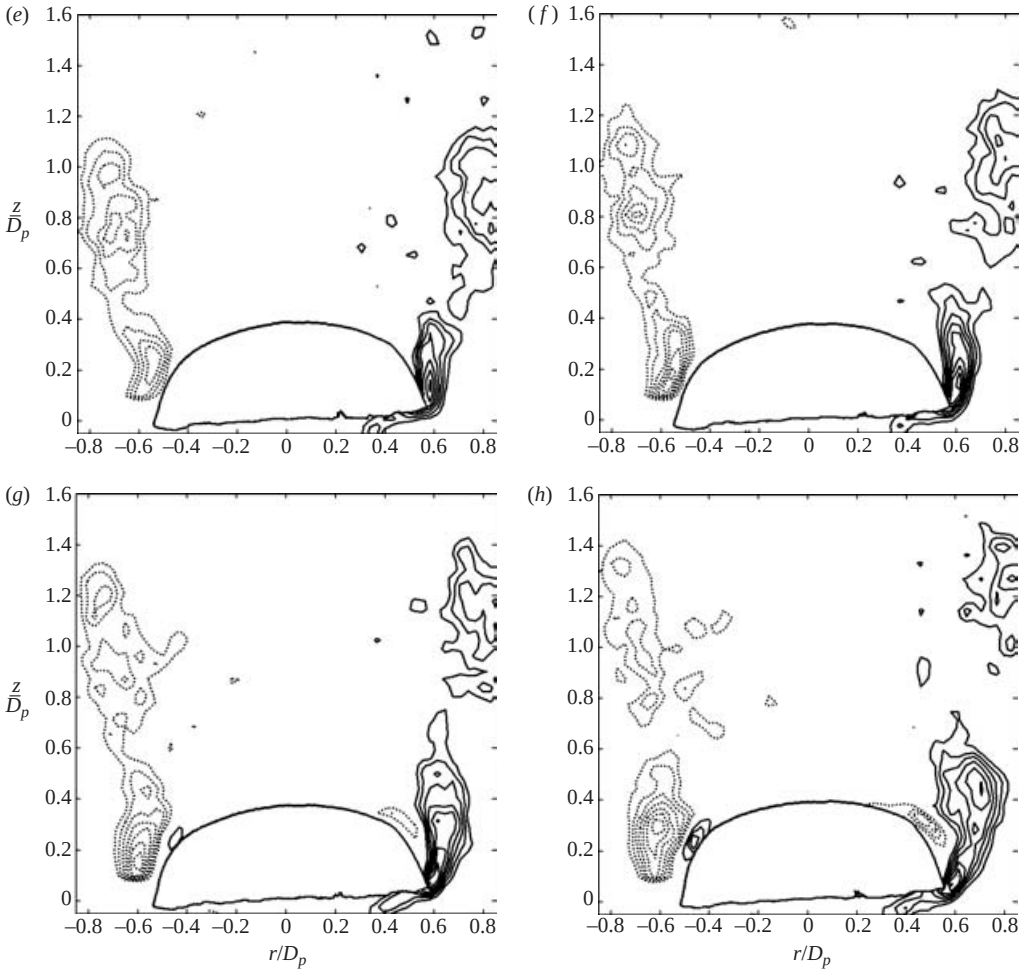

FIGURE 13. Phase-averaged vorticity fields for the 15 cm canopy at (*a*) 24°, (*b*) 72°, (*c*) 96°, (*d*) 144°, (*e*) 192°, (*f*) 240°, (*g*) 288° and (*h*) 336°. Solid and dashed contours indicate positive (counterclockwise) and negative (clockwise) vorticity. The lowest vorticity contour is at $|\omega D_p/U| = 3.0$ with increments of 1.5.

The peak vorticity, core position and circulation of the rolled up vortices were measured from the phase-averaged fields. The peak vorticity is plotted in figure 14 for the primary vortex visible in all 15 phases. The data show a decreasing peak vorticity as the vortex progresses downstream. Also plotted in figure 14 is the shortest distance, *s*, between the vortex core and the canopy surface. It turned out that the shortest distance was typically between the core and the canopy 'shoulder' area (the area beneath the opposite signed vorticity). The distance *s* is required in order to estimate the suction pressure imposed on the canopy surface by the rolled up vortices. As expected, *s* increases with the downstream progression of the primary vortex. The vortex circulation could not be completely accounted for in the phases where the vortex started to drift outside the boundary, see figure 13(*d–h*). For cases where a portion of the vortex was outside the boundary, the circulation was estimated by assuming the vortex core to have a Gaussian distribution of radius *a*. The latter was estimated from the available vorticity distribution. Thus, the circulation was

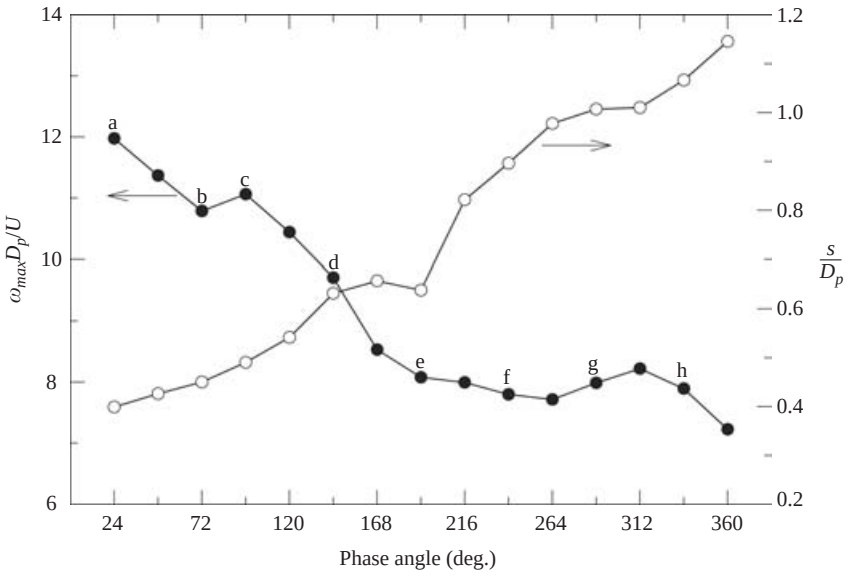

FIGURE 14. Maximum vorticity (filled symbols) and shortest distance (open symbols) between the vortex core and the canopy surface as a function of phase angle for the 15 cm canopy at $Re \approx 3.0 \times 10^4$. Letters refer to the phases in figure 13.

computed for these cases by $\Gamma \approx \pi a^2 \omega_{max}$. The vortex radius a increased from about 1.3 to 1.8 cm for the vortex cores in figure 13.

To relate breathing of the canopy with the near-wake vortex dynamics, we attempted to correlate the position and circulation Γ of the rolled up primary vortex with the canopy motions. The breathing is expected to be a result of the pressure variations on the exterior surface of the canopy since pressure on the interior surface is almost at the stagnation value (Johari, Stein & Tezduyar 2001). Neither the vortex core location nor the circulation could individually be correlated with the maximum canopy diameter. To estimate the relative variation of the pressure on the canopy surface, we used the expression for the pressure field of a free vortex, i.e.

$$p - p_\infty = -\frac{\rho \Gamma^2}{8 \pi^2 s^2}.$$

The estimated maximum suction pressure coefficient, $-Cp_{max} = (\Gamma/2\pi s U)^2$, on the canopy surface, derived from the above expression, is plotted against the maximum canopy diameter in figure 15. The vortex properties are those from the right-hand side of the vorticity fields; the secondary counter-rotating vortices and other small-scale vortices are excluded here. Only the circulation associated with the primary rolled up vortex core is accounted for in the suction pressure estimates; the circulation of the subsequent vortex (see figure 13*h*) is ignored. The data in figure 15 indicate a clear dependence of the maximum diameter on the estimated surface pressure. As the suction is reduced, the canopy expands to its maximum diameter. Increased $-Cp_{max}$ brings about reduced canopy diameters. It should be noted that suction pressure acts primarily on the canopy 'shoulder', and away from the skirt. Thus, increased $-Cp_{max}$ pulls the upper portion of the canopy in the axial direction, causing a reduction in the canopy maximum diameter. Removal of the suction pressure results in the canopy reaching its maximum diameter. Note that there are other vortices in the field that contribute to the surface pressure and which are not taken into account;

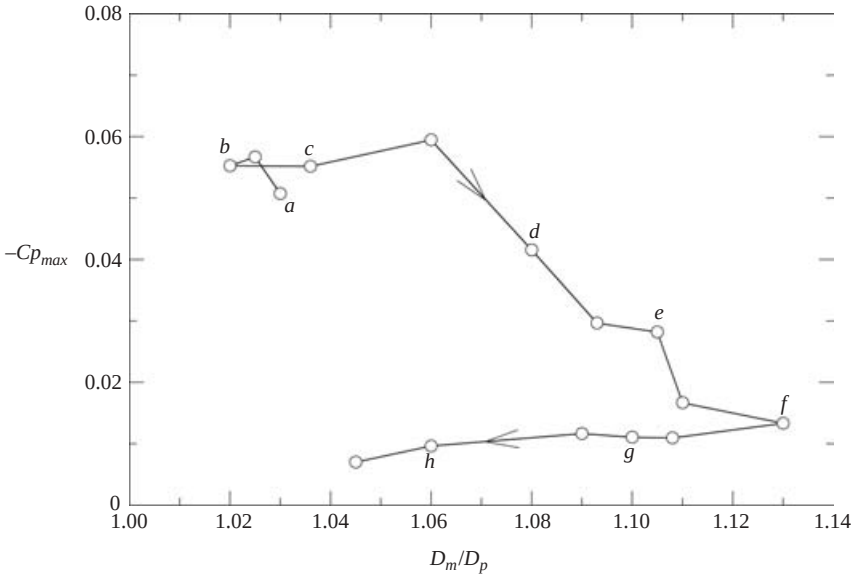

FIGURE 15. Maximum suction pressure coefficient on the canopy surface as a function of canopy maximum diameter for the 15 cm canopy at $Re \approx 3.0 \times 10^4$. Letters refer to the phases in figure 13.

see for example the vortex core in the upper right-hand corner and the secondary vortex in figure 13(*a*). Even though the computed maximum suction pressure is only an estimate, we believe that it provides sufficient evidence for the direct correlation between the canopy breathing and near-wake vortex dynamics.

4.5. *Drag*

Drag on the canopy was measured by a load cell in the forebody, and is normalized by the corrected dynamic pressure and the mean canopy projected area ($\pi D_p^2/4$). No correction for the forebody wake effects was applied. Drag coefficient for the 15 cm canopy at $Re \approx 3.0 \times 10^4$ is shown in figure 16 for a period corresponding to approximately four breathing cycles. Simultaneous measurements of the maximum canopy diameter are also plotted in figure 16. Evident are large departures of drag from its mean, with a standard deviation equal to 27 % of the mean drag. Similar large fluctuations of drag were also recorded for all cased examined here. In contrast to common belief (Knacke 1992), the drag fluctuations do not appear to be a direct result of the canopy diameter oscillations. The peaks in drag are not at the same instants as the peaks in diameter. The canopy diameter oscillations are periodic with a standard deviation of ~ 4.5 % of the mean value. Thus, a simple calculation of drag with the varying canopy area cannot explain the 27 % standard deviation. Moreover, computation of the correlation coefficient between drag and canopy diameter, based on ~ 40 breathing cycles, revealed a weak negative correlation (-0.14) at the lowest Reynolds number, and an even smaller positive correlation ($+0.06$) at the highest $Re \approx 6.0 \times 10^4$. Hence, another source seems to be responsible for the measured drag fluctuations.

The relative effect of canopy diameter oscillations on the drag fluctuations was examined through the component stemming from the unsteady potential flow around the canopy. Although potential flow drag is commonly associated with free-stream acceleration, the former is also present in steady flow around an expanding object.

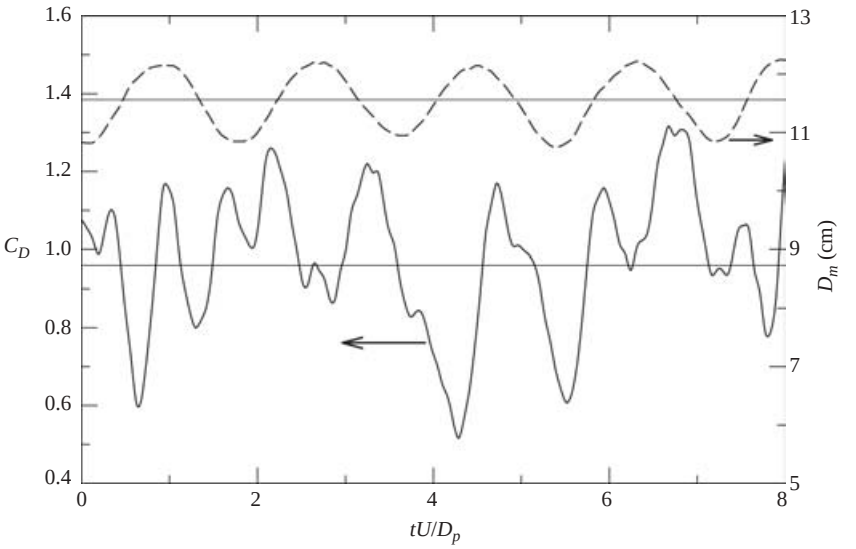

FIGURE 16. Drag coefficient (solid) and canopy maximum diameter (dashed) as a function of time for the 15 cm canopy at $Re \approx 3.0 \times 10^4$. Horizontal lines indicate the average values.

For a spherical bubble expanding in rectilinear flow, Ohl, Tijink & Prosperetti (2003) found the potential flow drag to be $0.5\rho\dot{V}U$. Here, $\dot{V}$ represents the rate of bubble volume expansion.

Potential flow calculations of Ibrahim (1967) for a rigid hemispherical cup resulted in a drag of $4.475\rho R^3\dot{U}$, where R is the hemisphere radius. This expression can be rewritten as $2.14\rho V\dot{U}$, with V representing the enclosed volume of the hemisphere. Thus, a hemisphere has an added mass of $2.14\rho V$. If we assume the canopy can be approximated as a hemispherical cup, then the force contributed by the added mass for a flexible hemisphere in steady flow would be $F_{am} \approx \mathrm{d}(2.14\rho VU)/\mathrm{d}t = 2.14\rho\dot{V}U$, where $\dot{V}$ is the time rate of change of the enclosed volume.

The force on the canopy contributed by the added mass term was found from the time history of the volume enclosed by the canopy. The volume was computed from the measured instantaneous boundary, assuming a body of revolution formed by the imaged two-dimensional canopy slice. As expected, the enclosed volume also oscillated periodically at the breathing frequency. The sign of F_{am} changes as the canopy expands and contracts during each cycle, resulting in a mean value of zero. The r.m.s. value of F_{am} was found to be 39.8 % of the measured drag standard deviation at $Re \approx 3.0 \times 10^4$. This ratio decreased to 21.3 % as the Reynolds number was increased to 6.0×10^4 for the smaller model. The r.m.s. value of F_{am} for the larger model was 9.3 % of the measured drag fluctuations. The relative contribution of F_{am} fluctuations to the drag fluctuations seems to depend on both the Reynolds number, as inferred from the smaller model data, and mass ratio, comparing the large and small models, for the cases examined here. Data over a broader range of these parameters is required to elucidate conclusively their separate effects on the F_{am} variations. Aside from these considerations, the added mass appears to play a role in the drag fluctuations, at least for the small models in the present experiments.

Spectral analysis of the drag time series showed peaks corresponding to Strouhal numbers of 0.16 and 0.57. The latter is associated with the canopy breathing/vortex-shedding mode discussed earlier. The $St \approx 0.16$ is the same as that found in the radial

velocity data, and is consistent with the asymmetrical mode observed in disk wakes (Berger *et al.* 1990).

5. Concluding remarks

It has been demonstrated that the shear layer emanating from the canopy rolls up and forms a symmetric vortex ring within the first mean projected diameter from the canopy skirt. Subsequently, the vortex separates from the shear layer and is shed. The roll-up and shedding process occurs at a Strouhal number of 0.55, higher than any previously reported value for disks and spheres. The normalized breathing frequency of the canopy also has the same value, indicating the direct relationship between vortex shedding and canopy breathing. The observed Strouhal number is independent of Reynolds number within the range investigated here, and furthermore, may be only weakly *Re* dependent at Reynolds numbers up to $\sim 10^7$. Full-scale canopies have normalized breathing frequencies approximately 10 % lower than the value for the models employed in our study. The reduced breathing frequency is a weak function of canopy stiffness and/or Reynolds number.

The relationship between vortex shedding and canopy breathing was shown to be through the variation of the suction pressure on the exterior surface of the canopy, caused by the cyclic formation and shedding of the vortices in the near wake. As the vortices pinch off from the shear layer and move away from the canopy surface, suction on the canopy surface is relieved and it expands to its maximum diameter. Minimum canopy diameter is associated with strong vortices being present close to the upper portion of the canopy. Even though canopy diameter variations and drag fluctuations are not directly correlated, canopy breathing affects drag indirectly through the added mass effect associated with the variations in the canopy enclosed volume.

The observation of vortex shedding in the near wake of parachute canopies having a Strouhal number much greater than those associated with disks (≈ 0.14) and spheres (≈ 0.2) in the same Reynolds-number range shows that flexible bluff bodies have different near-field characteristics. The low-inertia fabric readily responds to fluid-imposed pressure distribution and this creates a strong fluid–structure interaction in the near wake affecting vortex formation and dynamics. However, farther downstream, vortex characteristics in the canopy wake are expected to become similar to rigid bluff bodies. Evidence for emergence of a mode at Strouhal number ≈ 0.16 was seen in our data at 1.6 diameters downstream.

This work was funded by the US Army Research Office grant DAAG55-98-1-0171 under technical direction of Dr T. Doligalski. The assistance of Dr C. Lee and Mr R. Benney of the US Army Airdrop Technology Team is greatly appreciated. We also acknowledge the help of D. Bond and M. Patel with data processing.

REFERENCES

Achenbach, E. 1974 Vortex shedding from spheres. *J. Fluid Mech.* **62**, 209–221.

Berger, E., Scholz, D. & Schumm, M. 1990 Coherent vortex structures in the wake of a sphere and a circular disk at rest and under forced vibrations. *J. Fluids Struct.* **4**, 231–257.

Cockrell, D. J. 1987 The aerodynamics of parachutes. AGARD-AG-295.

Desabrais, K. J. 2002 Velocity field measurements in the near wake of a parachute canopy. PhD thesis, Mechanical Engineering Department, Worcester Polytechnic Institute, Worcester, MA, USA.

Fuchs, H. V., Mercker, E. & Michel, U. 1979 Large-scale coherent structures in the wake of axisymmetric bodies. *J. Fluid Mech.* **93**, 185–207.

Heinrich, H. G. & Hektner, T. R. 1971 Flexibility as a model parachute performance parameter. *J. Aircraft* **8**, 704–709.

Higuchi, H. 1991 Visual study on wakes behind solid and slotted axisymmetric bluff bodies. *J. Aircraft* **28**, 427–430.

Hoerner, S. F. 1965 *Fluid-Dynamic Drag*. S. F. Hoerner, Midland Park, NJ.

Ibrahim, S. K. 1967 Potential flowfield and added mass of the idealized hemispherical parachute. *J. Aircraft* **4**, 96–100.

Johari, H. & Desabrais, K. J. 2003 Stiffness scaling for solid cloth parachutes. *J. Aircraft* **40**, 631–638.

Johari, H., Stein, K. & Tezduyar, T. 2001 Impulsively started flow about a rigid parachute canopy. *J. Aircraft* **38**, 1102–1109.

Kim, H. J. & Durbin, P. A. 1988 Observations of the frequencies in a sphere wake and of drag increase by acoustic excitation. *Phys. Fluids* **31**, 3260–3265.

Klimas, P. C. & Rogers, D. F. 1977 Helium bubble survey of a parachute-opening flowfield using computer graphics techniques. *J. Aircraft* **14**, 952–958.

Knacke, T. W. 1992 *Parachute Recovery Systems Design Manual*. Para.

Lamberson, D., Higuchi, H. & van Rooij, M. 1999 Characteristics of flow within concave-nosed bodies. *Proc. 15th CEAS/AIAA Aerodyn. Deceleration Systems Technol. Conf. AIAA Paper* 99-1738.

Lee, C. K. 1989 Modeling of parachute opening: an experimental investigation. *J. Aircraft* **26**, 444–451.

Lingard, J. S. 1978 The aerodynamics of parachutes during the inflation process. PhD thesis, Department of Aeronautical Engineering, University of Bristol, UK.

Macha, J. M. & Buffington, R. J. 1989 An experimental investigation of wall-interference effects for parachutes in closed wind tunnels. *Sandia Rep.* SAND89-1485.

Maskell, E. C. 1965 A theory of blockage effects on bluff bodies and stalled wings in a closed wind tunnel. ARC R & M, Aeronautical Research Council, UK.

Maydew, R. C. & Peterson, C. W. 1991 Design and testing of high-performance parachutes. AGARD-AG-319.

Natarajan, R. & Acrivos, A. 1993 The instability of the steady flow past spheres and disks. *J. Fluid Mech.* **254**, 323–344.

Niemi, JR, E. E. 1990 An improved canopy stiffness scaling law for determining opening time of flat circular parachutes. *Proc. of the AIAA 8th Appl. Aerodyn. Conf. Portland, OR, USA*, pp. 201–212.

Ohl, C. D., Tijink, A. & Prosperetti, A. 2003 The added mass of an expanding bubble. *J. Fluid Mech.* **482**, 271–290.

Pao, H.-P. & Kao, T. W. 1977 Vortex structure in the wake of a sphere. *Phys. Fluids* **20**, 187–191.

Peterson, C. W., Strickland, J. H. & Higuchi, H. 1996 The fluid dynamics of parachute inflation. *Annu. Rev. Fluid Mech.* **28**, 361–387.

Rae, W. H. & Pope, A. 1984 *Low-Speed Wind Tunnel Testing*, 2nd edn. John Wiley.

Raffel, M., Willert, C. E. & Kompenhans, J. 1998 *Particle Image Velocimetry – A Practical Guide*. Springer.

Sakamoto, H. & Haniu, H. 1990 A study of vortex shedding from spheres in a uniform flow. *Trans. ASME* I: *J. Fluids Engng* **112**, 386–392.

Strickland, J. H. & Higuchi, H. 1996 Parachute aerodynamics: an assessment of prediction capability. *J. Aircraft* **33**, 241–252.

Taneda, S. 1978 Visual observations of the flow past a sphere at Reynolds numbers between 10^4 and 10^6. *J. Fluid Mech.* **85**, 187–192.

Weber, T. & Garrard, W. L. 1982 Effects of flexibility on stability of small ribbon parachutes. *J. Aircraft* **19**, 692–694.

West, G. S. & Apelt, C. J. 1982 The effects of tunnel blockage and aspect ratio on the mean flow past a circular cylinder with Reynolds numbers between 10^4 and 10^5. *J. Fluid Mech.* **114**, 361–377.

Willert, C. & Gharib, M. 1991 Digital particle image velocimetry. *Exps. Fluids* **10**, 181–193.